Uncovering the symmetry of the induced ferroelectric phase transformation in polycrystalline barium titanate

Lucas Lemos da Silva[*,a], Kai-Yang Lee[a], Simon Petrick[a], Martin Etter[b], Alexander Schökel[b], Cesar Giovanni Chaves[c,d], Nilson Oliveira da Silva[e,f], Lalitha Kodumudi Venkataraman[g], Gunnar Picht[h], Michael J. Hoffmann[a], Manuel Hinterstein[a]*

[a]Institute for Applied Materials, Karlsruhe Institute of Technology, 76131 Karlsruhe, Germany

[b]Deutsches Elektronen-Synchrotron DESY, 22607 Hamburg, Germany

[c]Faculty 2: Computer Science and Engineering, Frankfurt University of Applied Sciences, 60318 Frankfurt am Main, Germany

[d]Department of Computer Engineering, Tallinn University of Technology, 12618 Tallinn, Estonia

[e]Federal Institute of Mato Grosso do Sul, 79240-000 Jardim, Brazil

[f]Institute of Astronomy, Geophysics and Atmospheric Sciences, University of São Paulo, 05508-090 São Paulo, Brazil

[g]Department of Materials and Earth Sciences, Technical University of Darmstadt, 64287 Darmstadt, Germany

[h]Robert Bosch GmbH, Corporate Sector Research and Advance Engineering, Advanced Technologies for Chemical and Biological Systems, Robert-Bosch-Campus 1 71272, Renningen, Germany

*Corresponding author: lucas.silva@kit.edu

Abstract

Microstructural design is a widespread approach to tailor the properties of functional materials, with the size effect being an effective constraint that modifies physical phenomena. In this work, we investigate the grain size effect on the properties and the electric field-induced phase transformation behaviour in barium titanate. A broad range of unimodal average grain size distribution between 0.4 µm and 15 µm were successfully sintered avoiding abnormal grain growth. Samples with a grain size close to the range of 1 to 2 µm, balancing microstructural strain, presence and mobility of domain walls to allow the field induced crystal phase transformation, showed optimal electromechanical and dielectric properties. By means of *in situ* high energy X-ray diffraction and a high-resolution multianalyser detector we distinguish and quantify a tetragonal-orthorhombic phase transformation induced by an electric field, providing unambiguous proof of this induced phase transformation. These results contribute to the understanding of fundamental questions about the piezoelectric effect in barium titanate and consequently other similar systems.

Introduction

Barium titanate ($BaTiO_3$ or BT) is widely studied as the model ferroelectric material. Showing a perovskite crystal structure and thus ferroelectric polarization, BT is an important functional ceramic for a broad range of applications, such as multilayer ceramic capacitors (MLCCs)[1,2].

Piezoceramics such as BT are able to convert mechanical energy into electrical energy and vice versa. Ferroelectrics are a special class of piezoelectrics which are characterized by spontaneous polarization that can be reoriented by the application of an electric field. This results in an electric field induced macroscopic strain S_{33}, which can be used for applications. Ferroelectrics consist of regions with uniform electrical polarization, known as ferroelectric domains. The phase transformation from cubic to tetragonal results in a distortion of the unit cell with an expansion of

the unit cell parameter *c*. This is accompanied by a polar displacement and the formation of a spontaneous polarisation. Due to this transformation, the resulting polarisation and distortion is compensated by the formation of ferroelectric domains. The interface between differently oriented domains is known as domain wall. External stimuli such as electric fields, mechanical stress or heat can cause the domains to reorient. When this domain switching occurs, the domain wall moves through the crystal lattice and the domain wall motion can be facilitated or hindered by point defects in the structure and internal stresses. During the transformation from the paraelectric to the ferroelectric phase upon cooling, the ferroelectric domains are formed in a polycrystal to relieve the internal stresses in the structure. An applied electric field or mechanical stress induces a range of mechanisms in ferroelectrics such as the intrinsic lattice strain, extrinsic domain switching and phase transformation[3–5].

With the high demand for ever smaller electronic devices, it is desirable that polycrystalline BT be processed into fine grained and dense microstructure. However, it is already well known that the grain size has a significant influence on the properties of ferroelectrics. Since the 1940s, several studies have been carried out on the subject[6–10].

A high relative permittivity (ε') is one of the main properties of a dielectric material. However, this property can suffer variations due to external stimuli, such as electric field, mechanical stress, and temperature. Therefore, not only a high ε' value is desired, but also a good stability *in operando*. Understanding the structural mechanisms that occur in the material under certain conditions is fundamental for device optimization, especially in BT, which is a model ferroelectric system.

At room temperature, a BT single crystal has an ε' of 170 in the [001] direction (unit cell *c* axis) and 4000 in the [010] and [100] directions (unit cell *a* axis)[11,12]. ε' in coarse-grained polycrystalline BT is about 1500. However, Kinoshita and Yamaji[7] reported that the dielectric constant in BT with an average grain size of 1.1 µm is about three times larger than in BT with a grain size of 53 µm. Fine-grained BT easily exceeds an ε' of 5000. Therefore, such a high ε' in polycrystalline BT cannot be explained mathematically[13] by the average of the values obtained from a single crystal. This led Buessen *et al.*[6] to the development of the internal stress model, which shows the relationship between the 90° domains and permittivity. A few years later, Arlt *et al.*[14] reported, that the width of the ferroelectric domains is proportional to the square root of the average grain size in BT with intermediate grain sizes.

However, a well-known challenge in perovskite processing is abnormal grain growth during sintering[15–17]. To solve this problem, some authors make slight modifications in the Ba/Ti ratio of the perovskite BT structure, using dopants, modified atmosphere, or applying elaborate sintering techniques. Bäurer *et al.*[15] demonstrated in their study that BT with excess barium suppresses abnormal grain growth. Karaki *et al.*[18] demonstrated that it is possible to obtain fine grained, dense BT using two-step sintering in a common sintering furnace. Several other authors obtained BT using spark plasma sintering (SPS).[19–21] Some authors reported that sintering of BT below the eutectic temperature, approximately 1320 °C, favours the growth of the {111} faceted twin grains making them giant in a finely grained matrix[22,23]. This report makes a quenched sintering plausible, which avoids this temperature range on heating and cooling of the sample. With controlled BT processing, it is possible to produce polycrystalline ceramics with different average grain sizes and avoid abnormal grain growth.

In many well-known ferroelectric systems, the highest electromechanical properties are reached close to phase boundaries. These phase boundaries are usually dependent on material composition, temperature, and pressure. By means of external stimuli such as mechanical stresses or electric fields it is possible to induce a phase transformation[24–26]. The application of an external electric field to a ferroelectric material leads not only to domain switching but also to the distortion of the unit cell and phase transformations. Electric field-induced phase transformations were observed in a broad range of piezoceramics. These effects are frequently observed in materials with complex phase diagrams. Many works can be found in literature on these phase transformations in ferroelectric systems that

possess a morphotropic phase boundary, such as BNT-BT[27–32] or PZT[3,4,33–35], as well as in systems that exhibit a polymorphic phase boundary, such as $K_{0.5}Na_{0.5}NbO_3$[36–38] or $(Ba,Ca)(Zr,Ti)O_3$[39,40]. However, in solid solution end members the effect is less thoroughly investigated. Recently Zhang *et al.*[41,42] reported the antiferroelectric to ferroelectric phase transformation induced by electric field in $NaNbO_3$ single compound that not possess polymorphic or morphotropic phase boundary.

Although BT is the model system of ferroelectricity, the induced phase transformation phenomenon has been relatively little addressed in the literature. A field induced phase transformation from the paraelectric to the ferroelectric phase was observed close to the Curie temperature[24]. Wada *et al.*[43] identified an electric field induced phase transformation when studying domains in BT single crystals. In their study, they proved the influence of the domains on the electromechanical properties and documented a transformation from tetragonal to orthorhombic at around 1 kV/mm and from orthorhombic to rhombohedral at around 3 kV/mm with an electric field applied in the [111] direction. Franzbach *et al.* reported indications of a tetragonal to orthorhombic phase transformation with the electric field applied in the [110] direction. For polycrystalline BT, Ghosh *et al.*[10] reported a fully reversible electric field induced polymorphic phase transformation in BT that occurs during strong electric field application, however the symmetry or other details of the phase was not identified due to low instrumental resolution. Kalyani *et al.*[44] found weak indications of an irreversible electric field induced phase transformation to orthorhombic symmetry. Even though the previously mentioned studies found indications of electric field induced phase transformations, unambiguous proofs and details of the strain mechanisms are still missing.

The tetragonal symmetry of BT where $a_T = b_T \neq c_T$ can be visualized in Figure 1a). The tetragonal phase is accompanied by the formation of ferroelectric domains. There are six possible directions for the domain orientations with either 90° or 180° between the polarisation directions (Figure 1b)). In its orthorhombic symmetry (Figure 1c)) the unit cell is differently set up and distorted with $a_O \neq b_O \neq c_O$. Here the a_O axis corresponds to a pseudocubic a_C axis. Both the b_O and c_O axes correspond to $<110>_C$ directions. Similar to the tetragonal phase, the polarisation direction is the $[001]_O$ direction. In Figure 1d) we can observe that in the orthorhombic symmetry twelve polarization directions are possible, forming domain walls of 60°, 90°, 120° and 180°.

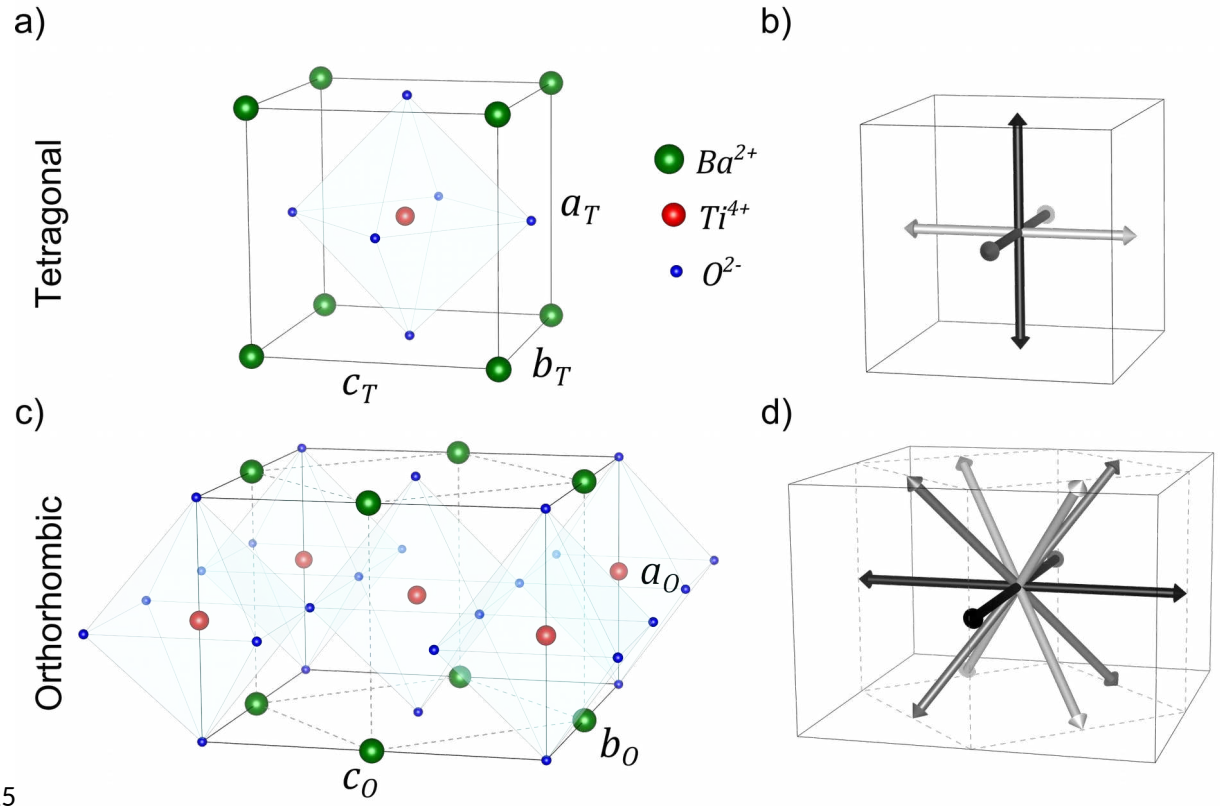

Figure 1: Schematic representation of the perovskite BT unit cell. (a) Tetragonal and (c) orthorhombic symmetries. The possible directions of spontaneous polarization are also represented for (b) tetragonal and (d) orthorhombic symmetry.

Since the dielectric and electromechanical properties as well as the structural behaviour of BT are highly dependent on grain size[10,14,45–49], we investigate in this study the grain size dependence in polycrystalline BT. In order to be able to determine a clear dependency, a narrow and uniform grain size distribution is mandatory. Since details on the structural response to an electric field are still missing, we investigate the field induced behaviour with high resolution synchrotron experiments. These results will be of high importance for the development of high performance dielectrics based on BT.

Experimental

Barium titanate samples were produced from ceramic powder (Alfa Aesar, 99%). In order to obtain different grain sizes and to avoid abnormal grain growth[15,16,22] the green bodies were sintered by three different methodologies: *two-step sintering*,[18,50,51] *quenched sintering*, and *spark plasma sintering (SPS)*. For two-step sintering and quenched sintering, cylindrical green body pellets were pre-pressed uniaxially at 30 MPa and cold isostatically pressed at 400 MPa. For SPS the green bodies were pre-pressed uniaxially in a cylindrical graphite matrix of 20 mm in diameter at 10 MPa. Details of the sintering parameters can be seen in Table 1. Subsequently the SPS samples were annealed in oxygen atmosphere at 1050°C for 32 hours in order to reoxidise and remove diffused carbon from the graphite matrices. After sintering, the samples were subjected to density analysis by the Archimedes method submerged in distilled water with a precision balance (Sartorius).

Table 1: Summary of sintered samples. The average grain size and the relative density are shown as well.

Sintering method	Atmosphere	Temperature (°C)	Time (min)	g_{mli} (µm)	Rel. Density (%)
Spark Plasma Sintering	Argon / Vacuum	1150	3	0.44(1)	99(2)
		1150	3	0.73(2)	95.9(1)
		1200	3	2.1(1)	98(1)
		1200	3	2.1(1)	97(2)
Quenched sintering	O_2	1325	5	0.84(3)	97(2)
		1330	20	9.2(3)	98.4(1)
		1355	20	15.1(4)	98.7(1)
Two-steps sintering	Air	1370 / 1150	1 / 900	9.1(3)	97.5(1)

The sintered samples were cut and embedded in 25 mm diameter cylindrical epoxy bodies and polished in diamond suspension down to 0.25 µm. Subsequently the samples were removed from the epoxy body and thermally etched at 1100 °C (fine grained samples) or 1200 °C (coarse grained samples) for 30 minutes in air. The etched samples were investigated with scanning electron microscopy (SEM, FEI NanoSEM) using a back-scattered electron detector. With the obtained images, the mean grain size was measured using the line intercept method, described in the technical standard DIN EN ISO 13383-1 and determined from the cutting line length (g_{mli}). To determine the grain size distribution with high statistics, the grain structures in the SEM images were skeletonized by hand and the resulting binary images were further analysed using functionality of MATLAB's Image Processing toolbox. The area of the individual grains was determined and used to calculate the equivalent circle diameter. To ensure reliability, at least 600 acquisitions were made in at least three different regions of the sample.

The electromechanical properties have been measured with a TF Analyzer 2000 (aixACCT). For this purpose, the samples were ground to a thickness close to 1 mm and on their parallel faces, gold electrodes were sputtered. The exact area of the electrodes was measured under a digital light microscope (Keyence). Immersed in silicone oil, the unpoled samples were subjected to a 2 kV/mm bipolar electric field with a frequency of 1 Hz. Subsequently five cycles of the same electric field were applied, and the data of the poled sample was collected. Subsequently the samples were subjected to small signal analysis to obtain the data of the piezoelectric coefficient (d_{33}) and relative permittivity (ε').

X-ray diffraction experiments were conducted in a conventional laboratory diffratometer (L-XRD) in reflection geometry, and at a high-energy synchrotron beamline (S-XRD) in transmission geometry. The main difference between the two geometries is that L-XRD returns information about the crystallographic structure near the surface of the samples while S-XRD refers to the bulk information as described by Kong *et al.*[52]. X-ray diffraction experiments with L-XRD were carried out on a Bruker D8 Advance diffractometer using Cu Kα radiation on the polished and thermally etched sample surfaces. X-ray diffraction experiments with S-XRD were conducted at the P02.1 beamline at DESY in Hamburg, Germany.[53] This beamline provides high energy (60keV) X-rays with a wavelength of 0.20718 Å. The experiment was conducted in transmission geometry in order to characterize the structural properties of the bulk. A 16-inch XRD 1621N ES Series (PerkinElmer) two-dimensional detector with a resolution of 2048x2048 pixels and 200µm² pixel size was used at a distance of 2250 mm from the sample in order to achieve high angular resolution[28,54]. More details on the experimental environment can be found in previous works.[27,55] The 2D data was divided in 5° sections and integrated in order to analyse the anisotropic effects of the applied electric field. More details can be found in the literature[28]. High resolution measurements were performed with the Multi-Analyser Detector (MAD)[56] at sample orientations of ω = 0°, 15°, 30°, 45°, 60°, 75° and 90° in the static maximum applied field (2 kV/mm), unpoled, and remanent state (0 kV/mm).

The STRAP (Strain, Texture, and Rietveld Analysis for Piezoceramics[3]) analysis was performed as reported in the literature[3,4]. In an initial refinement of the unpoled state, the atomic positions, lattice parameters as well as microstrain and size parameters were refined. For the STRAP analysis, the lattice parameters, lattice strain and texture parameters were refined. In order to account for the phase transformation, the scale parameters of the individual phases were refined and a linear interpolated background function accounted for the background. More details about the STRAP analysis can be found elsewhere[3,4]. The 2D detector offers high statistics and texture information. The MAD, despite the low statistics, has very high angular resolution that allows the detection of reflections that are very close or that are overlapping in the 2D data.

Results

The samples obtained and analysed in this work are listed in Table 1, as well as their respective average grain size obtained by the line intercept method and their relative densities measured by the Archimedes method. Figure 2a)-f) depicts the microstructure of the samples obtained by the different sintering methods. The microstructures show a high density with low porosity and grain sizes with a narrow and unimodal grain size distribution in the range from 0.4 to 15.1 µm (Figure 2g)). The data obtained by the line intercept method were weighted by length and used to plot the density distribution curve in Figure 2g). No bimodal grain size distribution appeared, indicating that abnormal grain growth has been successfully prevented with the preparation methods used in this work.

For BT at room temperature several authors[10,14,45–49] have already reported the dependence of electromechanical properties on grain size. The maximum of the relative permittivity values, reported in the literature, varies with grain sizes from 0.6 µm[49] to 2.0 µm[10], with the vast majority concentrating around 1 µm grain size. This discrepancy may be related to the methodology used in

grain size determination, stoichiometry[57] and processing. Buscaglia and Randall[8] report that the high relative permittivity values are due to the *mobility of the domain walls* and the high *domain wall densities* in this grain size range. Both the decrease and the increase in the size of the grains cause an attenuation in the electromechanical properties, but for different reasons. With the decrease in grain size, the mobility of the domain walls decrease due to the *clamping effect* of the grain boundaries. The increase in grain size reduces the domain wall densities, where according to Arlt *et al.*[14], the width of the domains is proportional to the square root of the grain size. In this work, this grain size range between 0.6 and 2 µm will be highlighted and will be called the grain **S**ize range of higher domain wall **D**ensity and **M**obility (SDM).

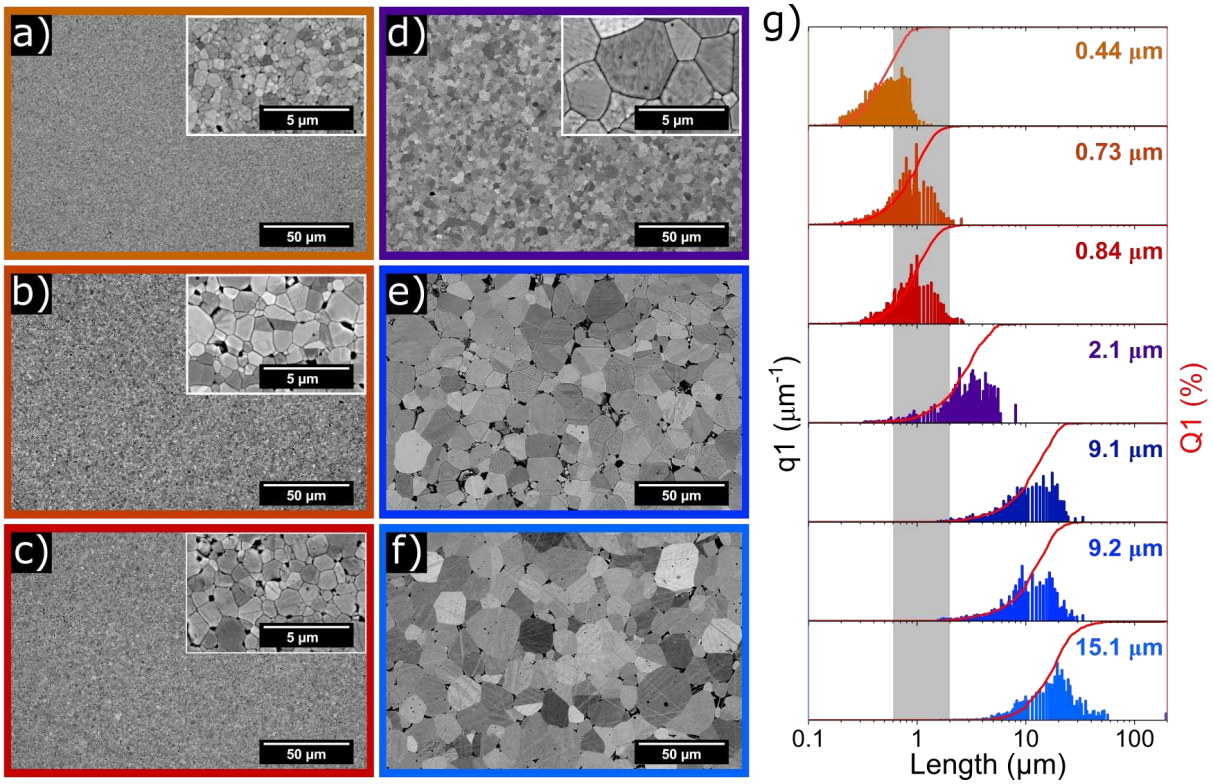

Figure 2: Microstructure of the samples. With an average grain size (a) 0.44 µm, (b) 0.73 µm, (c) 0.84µm, (d) 2.1 µm, (e) 9.1 µm and (f) 15.1µm. (g) Grain size distribution (q1) and cumulative distribution (Q1). Grain sizes are weighted by intercept length. The grey shaded region indicates the grain size distribution range for higher domain wall density and mobility.

Figure 3 shows the diffraction patterns of three unpoled samples from reflection (L-XRD) and transmission geometry (S-XRD). All samples appear as single tetragonal phase with no secondary phase reflections. With decreasing grain size, the tetragonal reflection splitting of the 200_C reflection (002_T and 200_T) decreases and the reflections are broadened. In the following, the subscripts T, O and C indicate tetragonal, orthorhombic and cubic indexing. While the reflection broadening is an effect of decreasing grain size due to size effects in diffraction, the reduced reflection splitting results from increasing stresses and reduced domain sizes as recently described in the literature[8,9]. Another effect that occurs simultaneously with the grain size reduction below 1 µm is the increase in temperature of the tetragonal-orthorhombic phase transformation that occurs between 0 and 10 °C for coarse grained BT[58]. For grain sizes smaller than 0.3 µm this transformation occurs around 20 °C[5,58]. As shown in Figure 2 the ceramic is composed of a grain size distribution, naturally just a portion of these grains suffer this effect.

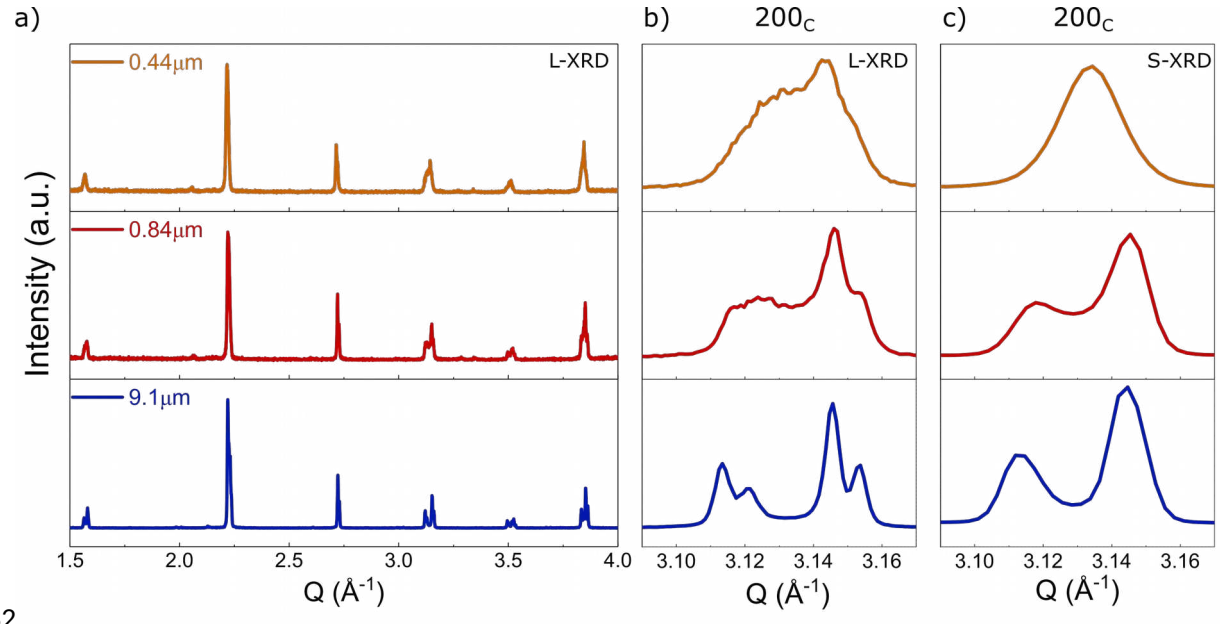

232
233*Figure 3: Diffraction patterns from different geometries. For samples with grain sizes of 0.4, 0.8 and 8.5 µm. (a) Full* 234*diffraction pattern obtained from reflection geometry (L-XRD), (b) 002_T and 200_T reflections obtained from L-XRD and (c)* 235*002_T and 200_T reflections obtained from S-XRD.*

236The unit cell parameters obtained by Rietveld refinement and the calculated unit cell distortions are 237graphically shown in Figure 4a) and b) and summarised in Table S1 in the supplementary material. 238The samples with grain sizes above the SDM have similar lattice parameters and show no differences 239between S-XRD and L-XRD. For grain sizes below the SDM the unit cell distortion, η_T, decreases 240significantly. The samples within the SDM show the transformation between the large and the small 241grain sizes. From the unit cell parameters, the unit cell volume can be calculated (Figure 4c)). For 242small grain sizes the unit cell volume decreases significantly. The onset of this decrease is lower for 243bulk (S-XRD) than for the surface (L-XRD). This indicates additional stresses at the surface. From the 244unit cell volume, a quasi-hydrostatic pressure p_V can be calculated as recently shown for PZT[9]. This is 245possible using the Birch-Murnaghan equation of state[59]:

246
$$p(V)=\frac{3B_0}{2}\left[\left(\frac{V_0}{V}\right)^{\frac{7}{3}}-\left(\frac{V_0}{V}\right)^{\frac{5}{3}}\right],$$

247with V_0 = 64.403(4) Å^3 for a grain size of 16.5 µm and a bulk modulus B_0 = 135 GPa[60]. The calculated 248pressure is plotted in Figure 4d). For the bulk material (using S-XRD dataset), p_V increases to more 249than 300 MPa. This value is about an order of magnitude higher than the blocking force of barium 250titanate based ceramics[1]. This explains the reduced electromechanical response for the sample with 251a grain size 0.4 µm. However, this is exactly the stress range reported for BT based ceramics with 252dark field X-ray microscopy[61]. Here stresses up to 300 MPa were reported in areas with highest 253domain wall densities.

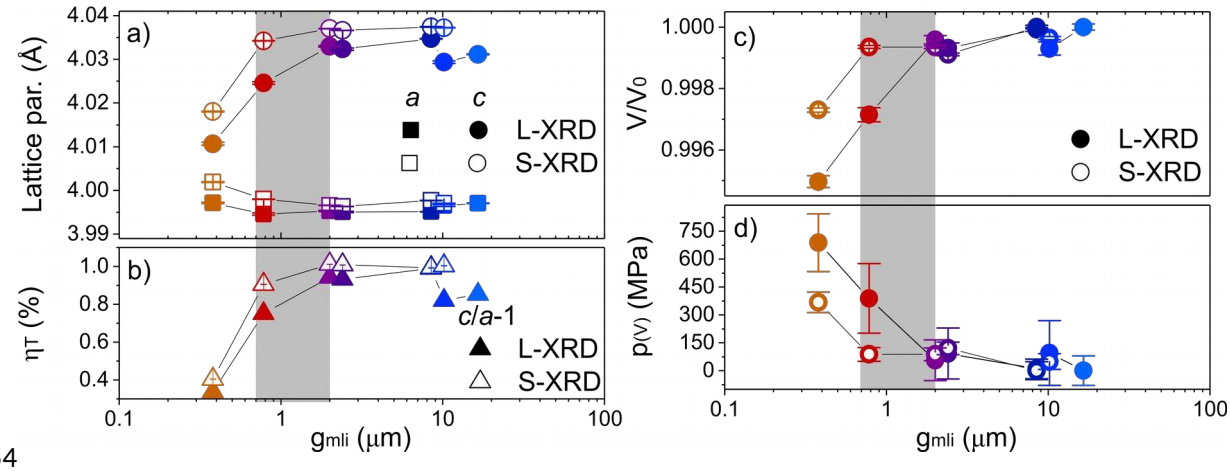

Figure 4: a) Lattice parameters obtained from Rietveld refinement, b) unit cell distortion (ηT), c) relative unit cell volume and d) recalculated quasihydrostatic pressure from L-XRD and S-XRD data.

The full polarisation, strain, piezoelectric coefficient and relative permittivity hystereses at room temperature are shown in Figure 5a)-d) for four representative samples. The mechanisms induced by the electric field are activated more easily for the 0.8 µm sample. This can be clearly seen by evaluating the d_{33} curve (Figure 5b)). For the 0.8 µm sample the d_{33} rapidly increases at lower electric field values. For samples with smaller or larger grain sizes this increase occurs at higher electric fields. This effect is also reflected in the polarization and strain curves (Figure 5a) and c)). On the other hand, in Figure 5d) the relative permittivity of the 0.8 µm sample, despite having the highest value, is drastically reduced by at least 70% upon application of the electric field. The coarse-grained 9.1 µm sample is more stable and suffers little effect of the electric field on the relative permittivity.

The relevant characteristic parameters extracted from measurements such as in Figure 5a)-d) are presented as a function of grain size in Figure 5e) – j). For the 0.7 and 0.8 µm grain size samples, values reach extrema. Most of the hystereses (Figure 5e) – i)) show the maximum value for a grain size of 0.8 µm. Samples with a larger or smaller grain size have smaller values. The coercive field E_C (Figure 5j)) shows the opposite behaviour. Here the minimum value can be found for the 0.8 µm sample. The results confirm the properties within the SDM. In the case of the BT composition used for this study, the maximum of the SDM can be found at grain sizes of 0.7 and 0.8 µm. Typical for more complex systems, the electric field induced phase transformation plays a crucial role in the development of ferroelectric properties. In BT it is possible that this phase transformation plays a relevant role dependent on the grain size. A highly complex behaviour and a broad range of field induced processes are elucidated with this study.

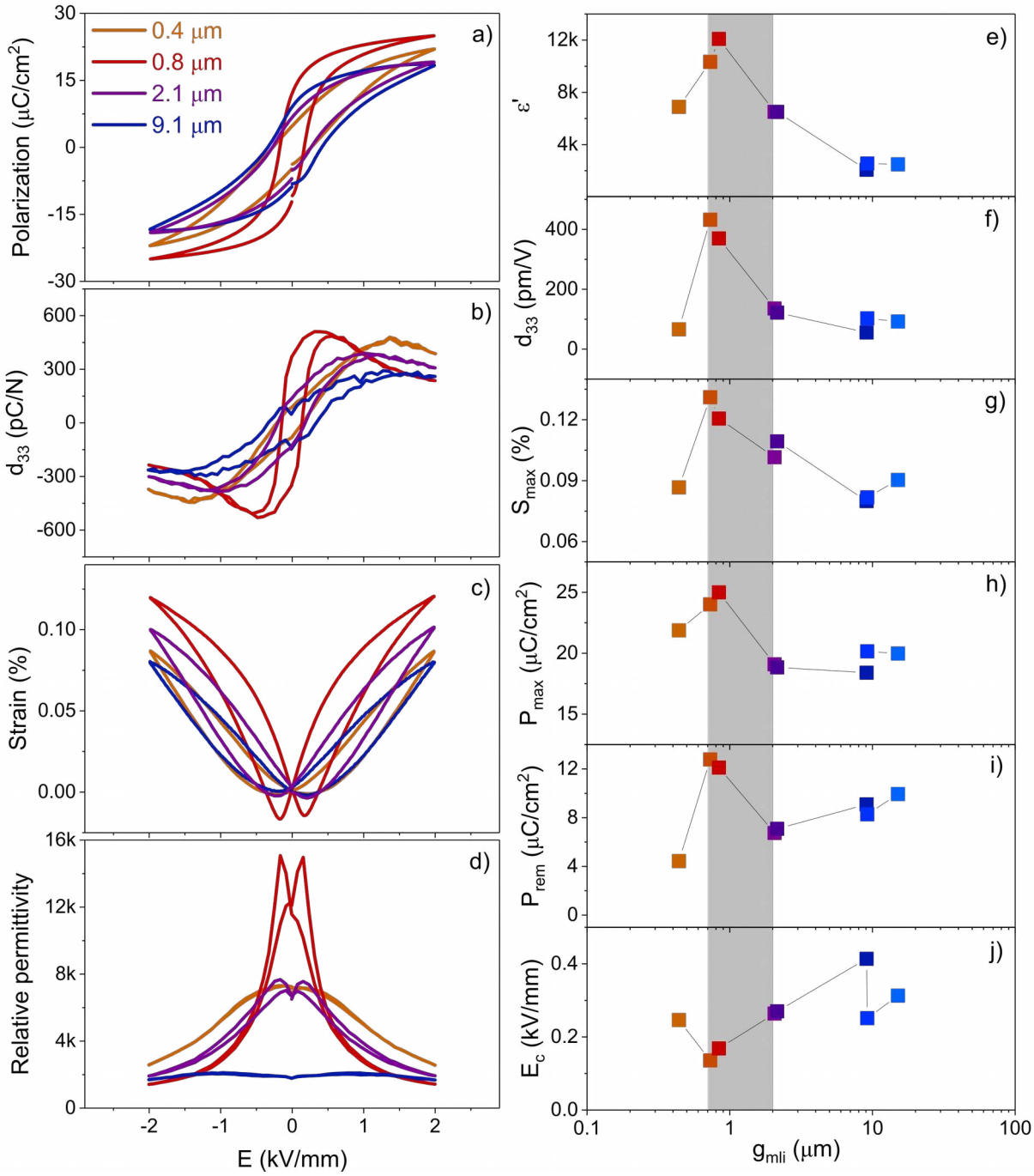

Figure 5: Electromechanical evaluation. Full hysteresis curves of a) polarization, b) piezoelectric coefficient, c) strain and d) permittivity for four representative samples. For all samples the values of e) relative permittivity ε', f) remanent piezoelectric coefficient $d_{33,rem}$, g) maximum strain S_{max}, h) maximum polarization P_{max}, i) remanent polarization P_{rem} and j) coercive field E_C. are shown.

In order to investigate the origin of the high properties in the SDM, more sophisticated structural studies are necessary. As Figure 3 shows, the reflections of the samples with small grain sizes are significantly broadened due to size effects and the high density of domain walls. However, for larger grain sizes, the reflections become sharper and a detailed structural study becomes feasible. The structural response to an applied electric field can be studied with *in situ* synchrotron experiments and the STRAP analysis[3]. In order to be able to distinguish the separate mechanisms and possible phase transformation, the reflection broadening from sample effects have to be minimized. The ideal compromise of pronounced response and small grain size can be found in a sample with grain size of around 2 µm.

Figure 6 shows the Rietveld refinement with data from the high-resolution MAD detector[62] from an unpoled sample with 2.1 µm grain size. In the Figure 7 shows the refinement with data from the 2D detector in high resolution distance of 2250 mm[54]. Both datasets were refined in a single refinement with a structure model of an orthorhombic *Amm*2 and a tetragonal *P*4*mm* phase. Results and agreement factors of the refinements can be found in Table 2. The MAD data shows that a single phase structure model would not be able to model the intensities between the split reflections such as the 110_C (Figure 6a)) or the 200_C (Figure 6c)) reflection. Note that the 2θ range of the 200_C reflection with 0.12° is twice as large as the range for the 110_C and 111_C reflection with 0.06°. Therefore, all parts of Figure 6 show the same magnification ratio. Here the orthorhombic phase accounts for additional intensity. In earlier publications on lead zirconate titanate (PZT) these intensities could be correlated with domain wall contributions and effects from domain morphologies[9,63,64].

Table 2: Refinement results and agreement factors for the unpoled, applied field and remanent state.

Parameter	Unpoled	2 kV/mm	Remanent
a_T	3.995447(5)	3.995230(13)	3.995387(6)
c_T	4.034841(15)	4.03408(3)	4.035315(12)
η_T	0.9860(5)	0.9723(11)	0.9993(5)
a_O	3.994877(15)	3.994372(16)	3.993970(17)
b_O	5.67921(5)	5.67242(3)	5.67382(2)
c_O	5.67891(3)	5.68683(4)	5.68617(4)
η_O	0.0054(14)	0.2540(11)	0.2176(12)
R_p	0.177	0.222	0.217
R_{wp}	0.101	0.170	0.154

The fit clearly shows that a single phase structure model insufficiently describes the observations, however, no distinct reflections appear that clearly indicate an orthorhombic secondary phase. From the literature it is well known that grain size effects[8] and stresses[65] might be able to shift the tetragonal to orthorhombic phase transformation temperature to higher values[5,58]. Stresses necessary for a significant shift of the transformation temperature may occur at domain walls and might influence the material behaviour for a high domain wall density[9]. However, the structure model should not be interpreted as a classical phase coexistence between a tetragonal and an orthorhombic phase in the unpoled state. The refined phase fractions in Table 3 indicate that this sample contains strong real structure contributions from domain walls. The orthorhombic phase fraction in the unpoled state has to interpreted as deviation from the long range average tetragonal structure. Since we determine more than 40% of this phase, this sample lies well in the SDM range and contains a high domain wall density, which explains the high properties, displayed in Figure 5e)-j).

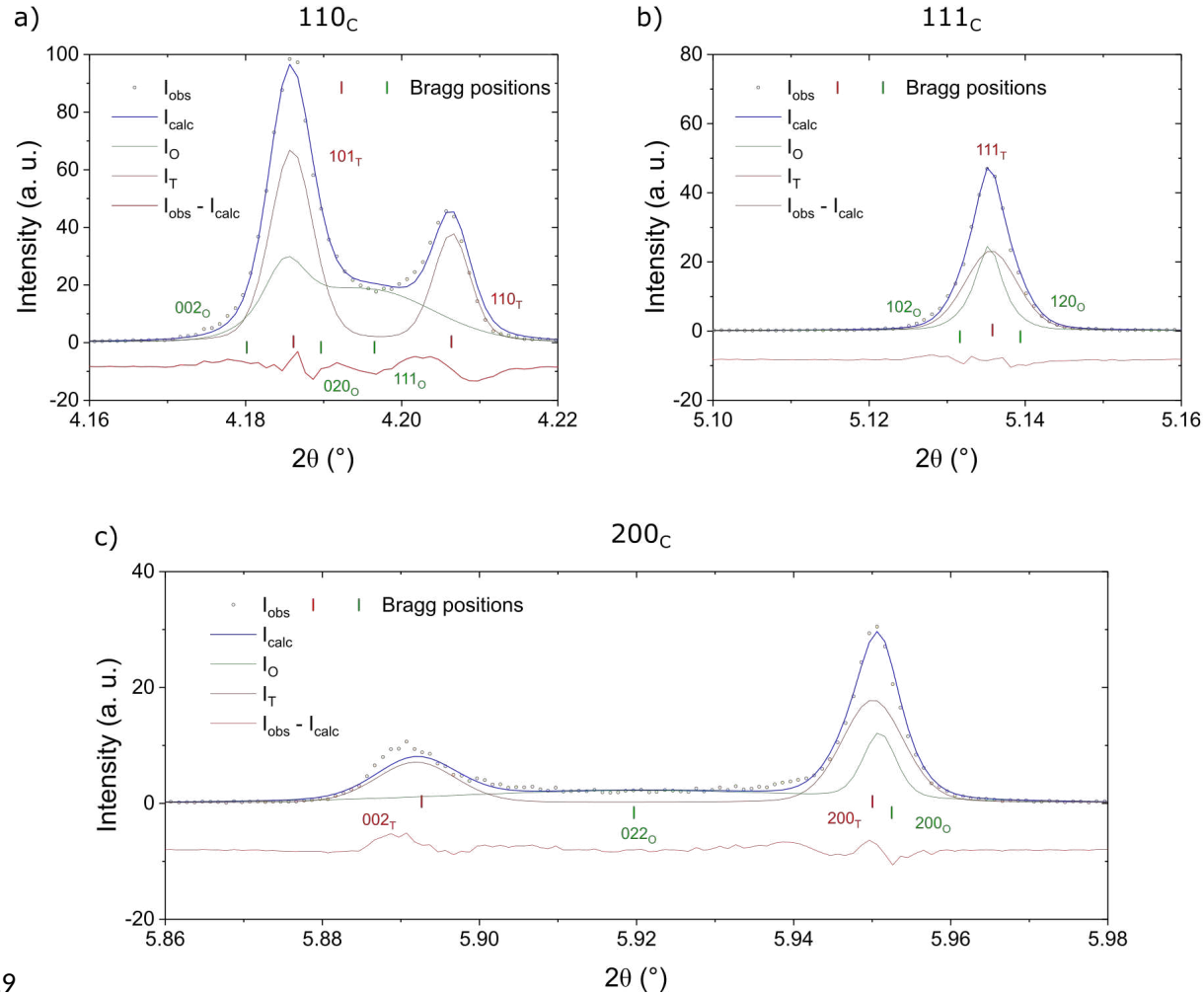

Figure 6: Refinement with high-resolution diffraction MAD data from an unpoled sample with 2.1 µm grain size. a) 110_C, b) 111_C and c) 200_C reflection. Structure model consist of an orthorhombic phase (I_O) and a tetragonal phase (I_T).

The refinement plots of the 2D data reveal the challenges of structural characterisation for fine grained BT (Figure 7). Note that here the 2θ ranges of the 110_C (Figure 7a)), 111_C (Figure 7b)) and 200_C (Figure 7c)) reflections are the same with 0.12°. Due to a significantly broader profile function, the reflection splitting of the 110_C reflection is less visible. With the 2D data alone, no justification for an orthorhombic secondary phase exists. However, refinement with the two-phase structural model explains the intensities appropriately. Nevertheless, the fit quality is significantly lower as it would be for a single phase refinement of the 2D data due to the significantly larger amount of data points in the MAD data set. This stresses the importance of the high-resolution data.

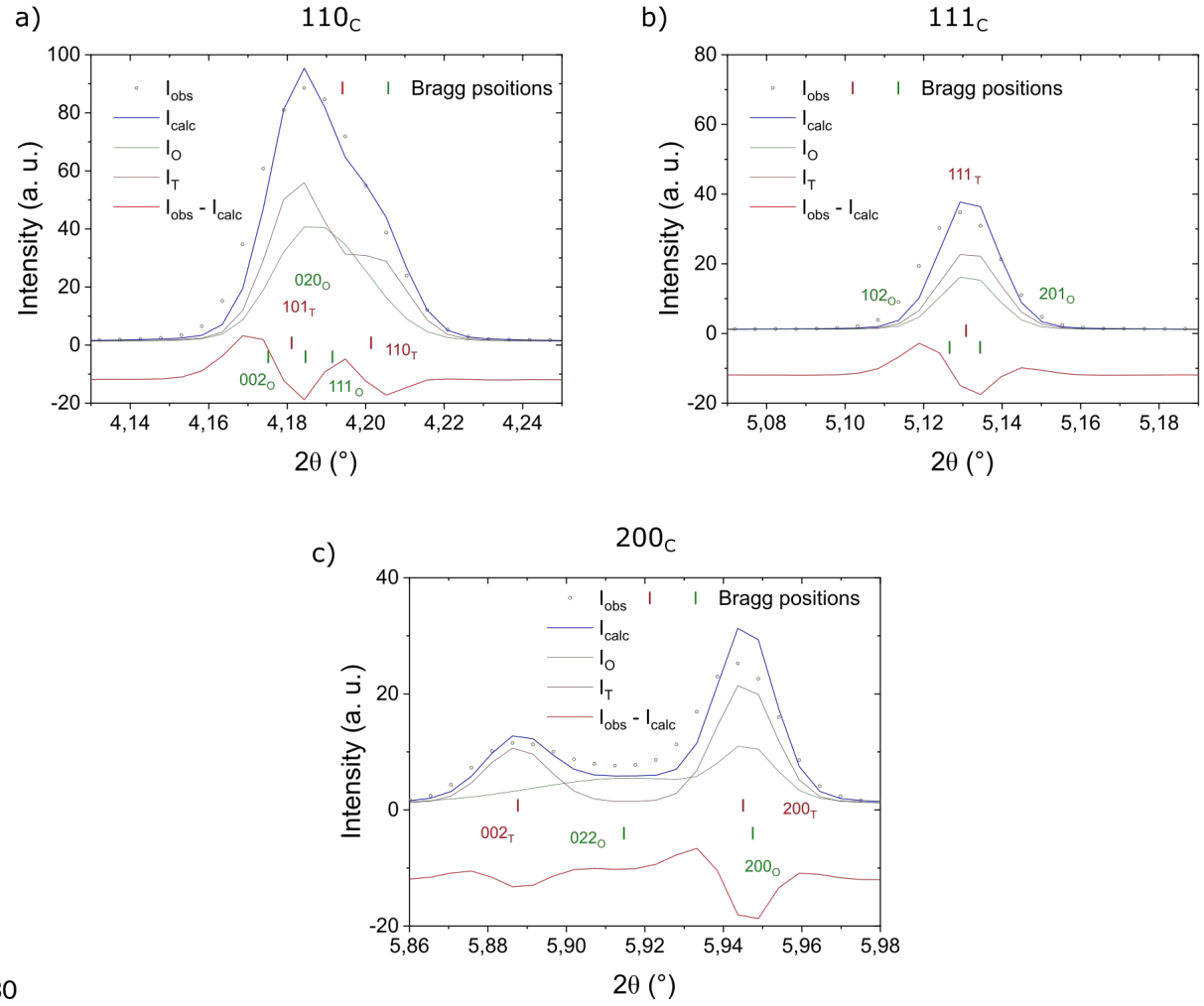

330

331*Figure 7: Refinement with 2D data from an unpoled sample with 2.1 µm grain size. a) 110_C, b) 111_C and c) 200_C reflection.*
332*Structure model consist of an orthorhombic phase (I_O) and a tetragonal phase (I_T).*

333Figure 8 shows the same reflections from the refinement with MAD data for a poled sample in the
334remanent state at 0 kV/mm. The same sample as in Figure 6 and Figure 7 was poled with 2 kV/mm in
335five bipolar cycles. Since the applied field induces texture, the sample orientation plays a crucial role.
336In Figure 8, the sample is oriented at ω = 45°. The two-phase structural model of an orthorhombic
337and a tetragonal phase is able to account for the observed reflection intensities. Especially, the 110_C
338reflection (Figure 8a)) shows distinct additional reflections for the orthorhombic phase. Also, the 111_C
339reflection (Figure 8b)) now shows a splitting, which is not allowed in tetragonal symmetry. The 200_C
340reflection only shows a slight increase in intensity between the tetragonal reflections (Figure 8c)). As
341previously observed for PZT[4,33,34], this reflection very well illustrates the field induced phase
342transformations and a similar effect was already reported for BT by Gosh *et al.*[10]. In our study the
343additional reflection, together with others, can clearly be interpreted as a ferroelectric orthorhombic
344phase, induced by the electric field. The sample still contains a high domain wall density, however,
345the orthorhombic phase was induced by the electric field and can be identified clearly by the
346observed reflections. The 2D data again is not able to reveal the details of the phase transformation
347due to the insufficient angular resolution (Supplemental information Figure S1).

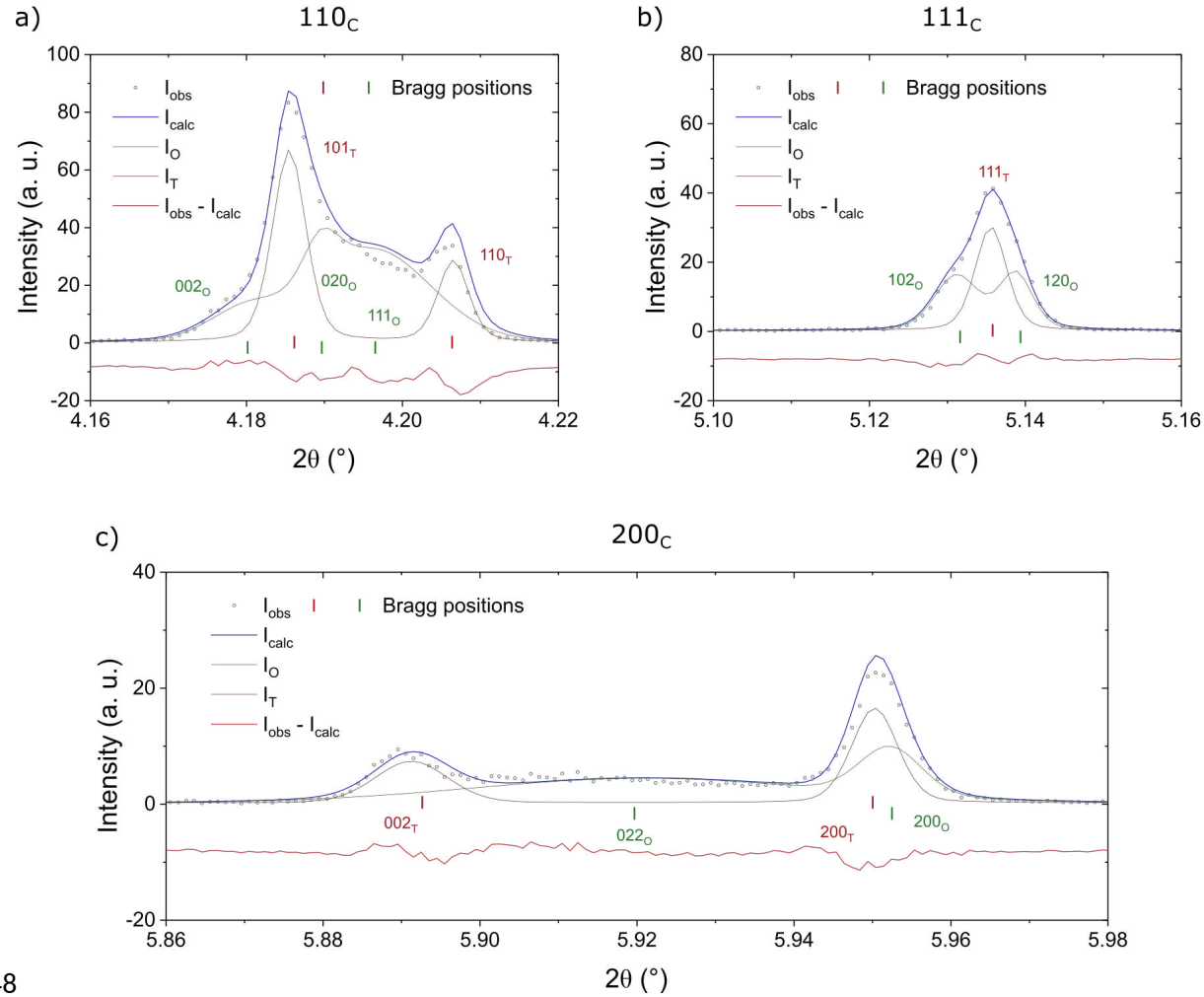

Figure 8: Refinement with high-resolution diffraction MAD data from a poled sample in the remanent state with 2.1 µm grain size. Sample orientation ω = 45°. a) 110_C, b) 111_C and c) 200_C reflection. Structure model consist of an orthorhombic phase (I_O) and a tetragonal phase (I_T).

When an electric field of 2 kV/mm is applied, the field induced phase transformation is more pronounced (Figure 9). Here the 110_C reflection clearly shows the distinct reflections of the orthorhombic phase (Figure 9a)). The splitting of the 111_C reflection increases significantly (Figure 9b)) and the additional intensity at the 200_C reflection can be clearly identified (Figure 9c)). The two-phase structural model of the STRAP refinement is able to account for all diffracted intensity. A representation of the data and refinements of all sample orientations of the characteristic 110_C reflection is shown in Figure 10. In great detail the refinement to other sample orientations ω = 90° and 0° can be achieved in the supplementary material (Figure S7 to S10). The results clearly show that the STRAP model can explain the field induced phase transformation from tetragonal to orthorhombic with applied electric field and that this is a crucial part of the response to an applied electric field. The STRAP analysis reveals an increase in orthorhombic phase fraction to 55.1(3)% in the remanent state at 0 kV/mm and 67.0(4)% in the applied field state at 2 kV/mm. Even when the 42.0(2)% are considered as domain wall contributions, this results in a change in phase fractions of 13.1% for the remanent and 25.0% for the applied field state.

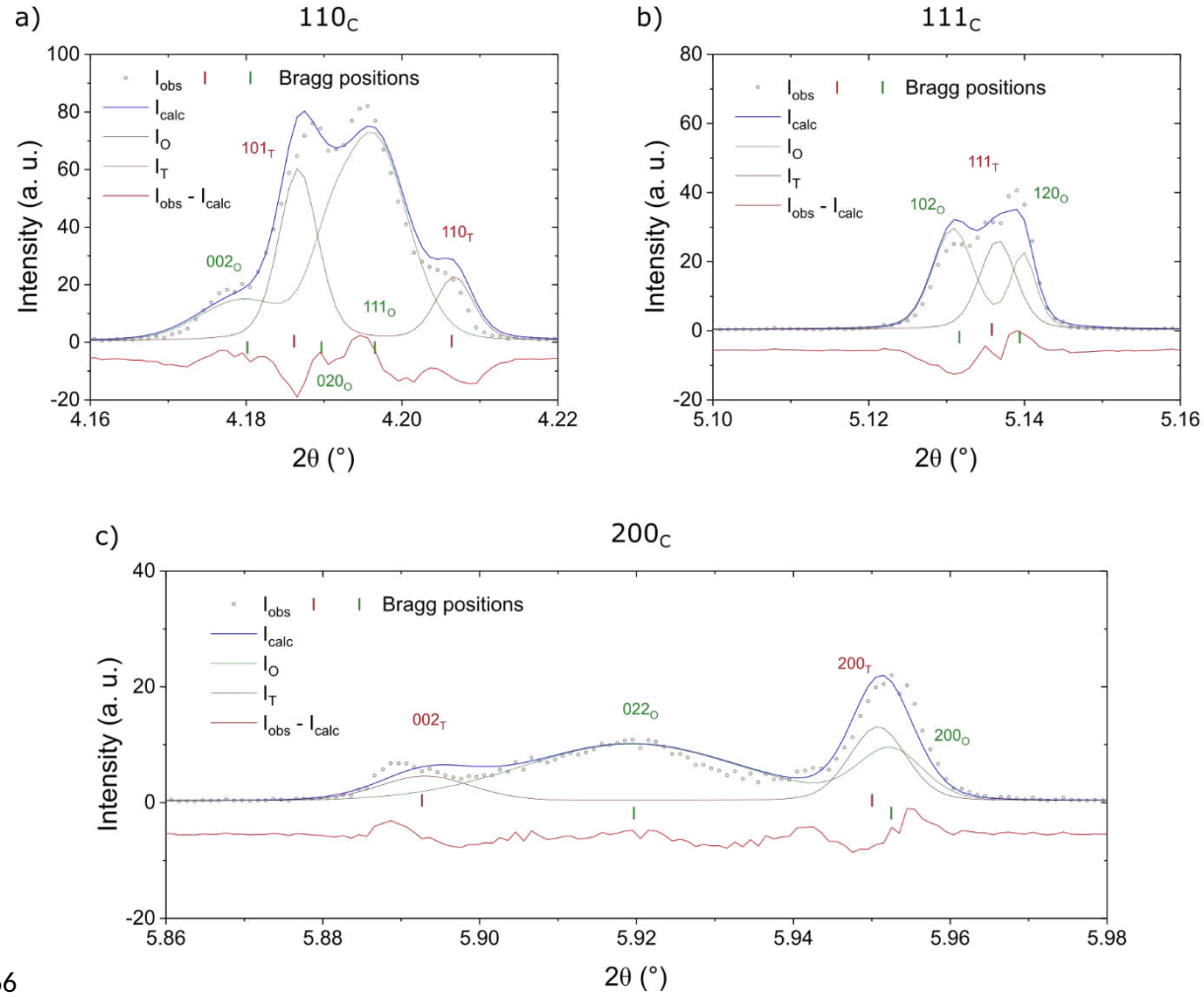

366

367*Figure 9: Refinement with high-resolution diffraction MAD data from a sample in the applied field state at 2 kV/mm with 2.1*
368*µm grain size. Sample orientation ω = 45°. a) 110_C, b) 111_C and c) 200_C reflection. Structure model consist of an*
369*orthorhombic phase (I_O) and a tetragonal phase (I_T).*

370Figure 10a) shows the diffraction data of the 110_C reflection, collected under the application of a
371maximum applied electric field of 2kV/mm. An electric field induced phase transformation in BT has
372been reported in the literature but has not been clarified. With this experiment we are able to
373elucidate the nature of the phase transformation. The two-phase structure model is able to account
374for the observed reflection intensities (b) with a tetragonal (c) and an orthorhombic phase (d).
375Especially the 110_C reflection shows distinct additional reflections for the orthorhombic phase.
376However, charts for the reflections 111_C and 200_C as well as for the remanent state can be seen in the
377supplementary material (Figures S2 to S6).

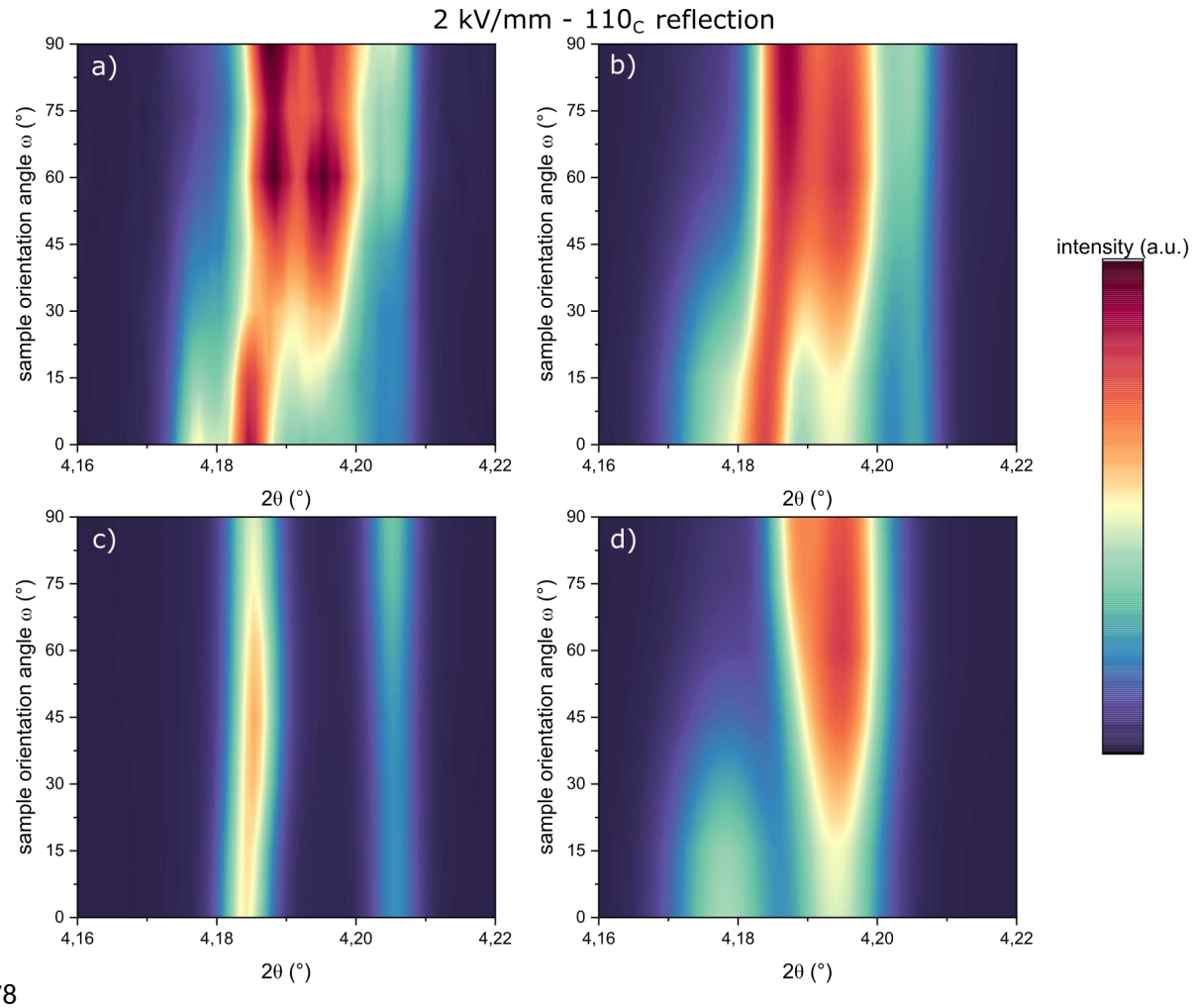

Figure 10: 2D plot correlating the angle ω and 2theta from 110_C reflection under an electric field from 2kV/mm. a) Data collected from MAD detector, b) refined two-phase model, c) refined tetragonal and d) refined orthorhombic phases.

As the results show, the sample with a grain size of 2.1 µm shows the most balanced appearance of sharp reflections and strong electric field induced phase transformation. However, the dielectric and electromechanical measurements indicate that the sample with a grain size of 0.8 µm exhibits highest properties (Figure 5e)-j)). When comparing the high-resolution MAD diffraction patterns of the samples with grain sizes of 2.1 µm and 0.8 µm, these maxima of highest properties are also reflected in a maximum of the field induced phase transformation (Figure 11). The 110_C reflection at around 2θ = 4.195°, the low angle 111_C reflection and the 200_C reflection between the 002_T and 200_T reflections are significantly stronger in the 0.8 µm sample than in the 2.1 µm sample. This indicates that the orthorhombic phase fraction increases dramatically under applied electric field in the 0.8 µm sample. The STRAP analysis reveals an orthorhombic phase fraction of 67.0(4)% for 2.1 µm and 82.3(1.0)% for 0.8 µm in the applied field state at 2 kV/mm. The summary of the quantified values of the electric field-induced phase as well as the maximum polarisation in the two main samples can be seen in the Table 3.

Table 3: Electric field induced phase fraction data on BT at two different grain sizes and their respective polarization values.

Grain size (µm)	Orthorhombic phase fraction (%)			Polarization (µC/cm²)	
	Unpoled	2 kV/mm	Remanent	2 kV/mm	Remanent
0.8	46.0(1.2)	82.3(1.0)	77.6(7)	25	12
2.1	42.0(2)	67.0(4)	55.1(3)	18	7

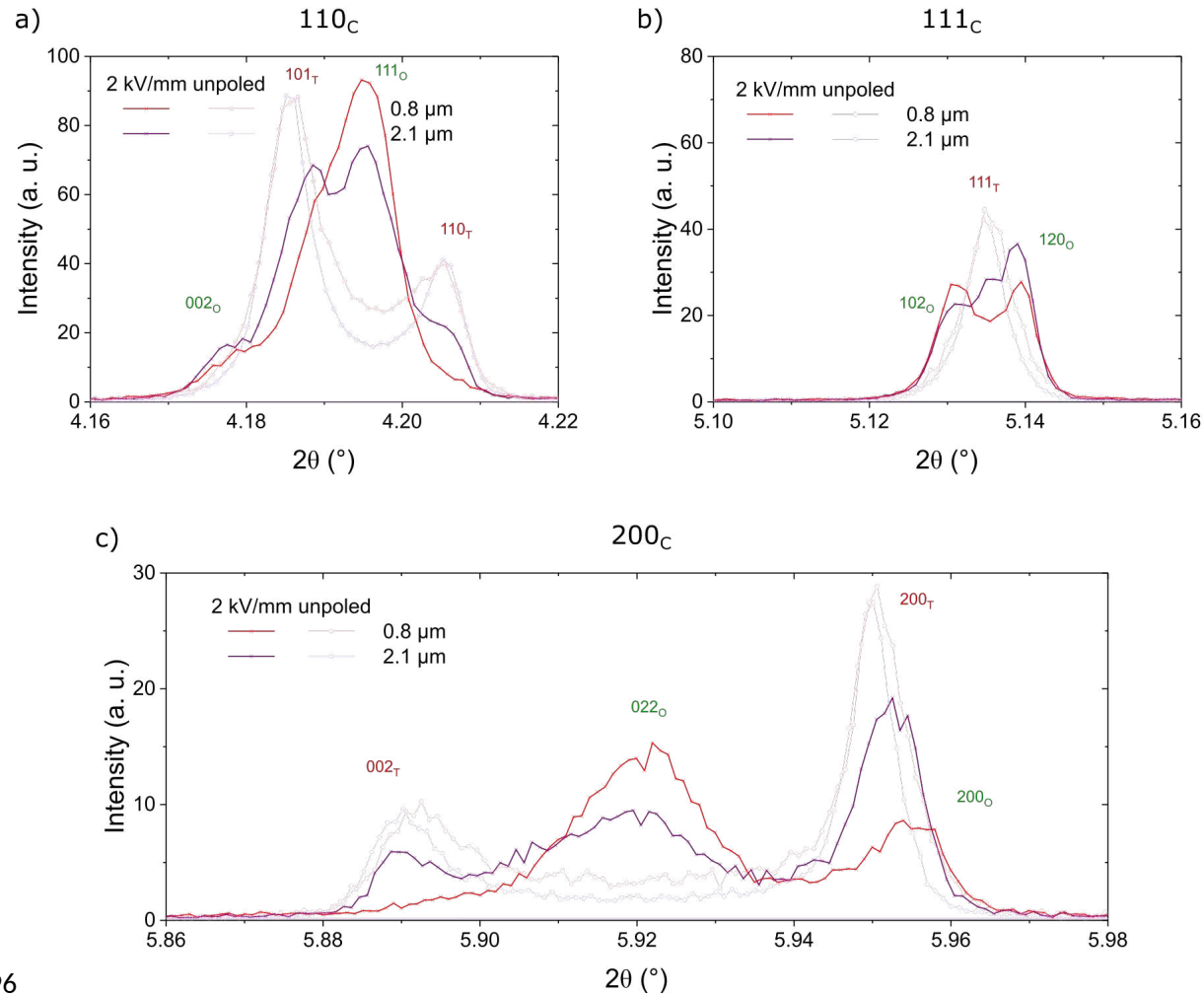

Figure 11: Comparison of high-resolution MAD diffraction patterns of two samples with grain sizes of 0.8 µm and 2.1 µm in the applied field state (2 kV/mm). a) the 110_C, b) the 111_C and c) the 200_C reflections at a sample orientation angle of $\omega = 45°$.

Under application of an electric (or elastic) field, the domain walls will move and their width will change, depending on the direction of the applied field and the direction of the polarization of the domains. Arlt *et al.*[66–68] proposed a mathematical model which proportionally relates the displacement of a 90° domain wall to the total deformation. That is, the electromechanical properties are better when a high domain density with high domain wall mobility is present. There is an optimal point where the internal stresses are high enough to generate a high amount of domains and low enough not to inhibit the mobility of the domain walls.

Unlike the brick wall model, the microstructure of polycrystalline barium titanate is characterised by a distribution of grain sizes and not by the repetition of grains of the same size, as can be seen in Figure 2 and schematically in Figure 12. The fraction of this grain size distribution that is within the SDM is determinant for achieving high electromechanical properties. Thus, in this work, the samples represented by the average grain size equal to 0.8 µm (quenched sintering) and 0.7 µm (spark plasma sintering), which have a grain size distribution mostly within the SDM, present the highest properties (Figure 5).

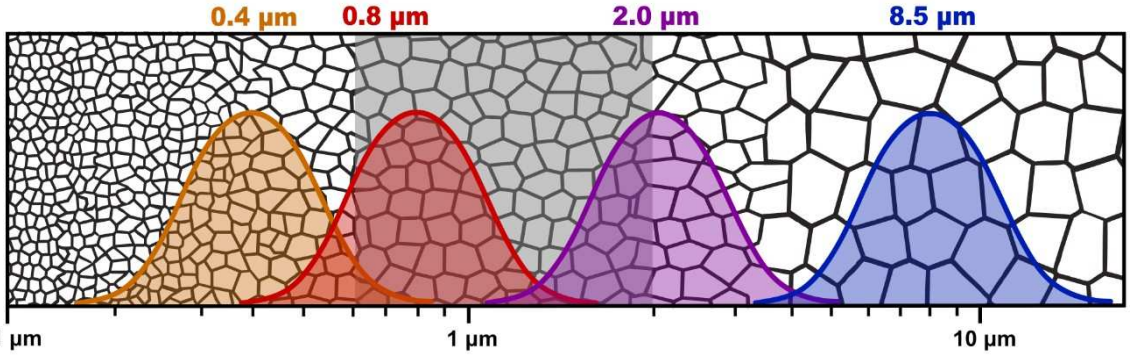

Figure 12: Representative design of the grain size fraction in the SDM, where the density and mobility of domains is greater.

The coexistence of the tetragonal and orthorhombic phases plays a crucial role for the high electromechanical properties. Phase distinction is impeded by the superposition of reflections (Figure 3) in samples with a grain size distribution below the SDM where internal stresses inhibit unit cell distortion (Figure 4). However, in the 2.1 µm sample, with a grain size distribution partially within and slightly above the SDM, it is possible to distinguish the coexistence of tetragonal and orthorhombic phases using the high resolution MAD detector and to quantify them using the STRAP method. Similar to lead zirconate titanate (PZT)[3,4] or bismuth sodium titanate[69,70] based ceramics, barium titanate also shows a coexistence of neighbouring thermodynamically stable phases. With this coexistence of phases, the origin of the enhanced electromechanical properties can be related analogously to systems with morphotropic phase boundaries where a lot of structural instability occurs. Damjanovic *et al.*[71,72] demonstrated that the presence of these instabilities create easy paths for rotation and extension of the polarisation vector in a flattened free energy profile. Since the lattice distortion decreases for smaller grain sizes and especially within the SDM (Figure 4b)), the activation energy of the field induced phase transformation is reduced. The increased domain wall density combined with the high mobility of the domain walls leads to a maximized response of an applied electric field. For grain sizes below the SDM, the influence of the domain walls on the crystal structure increases and as recently shown for PZT[9] and BT[61], the structure is subject to significant stresses (Figure 4d)). These stresses limit the domain wall mobility and also prevent the phase transformation. Additionally, the unit cell distortion decreases dramatically which is a prerequisite for a strong domain switching effect. Therefore, the combination of high domain wall density and mobility together with the electric field induced phase transformation is the origin of the maximum in properties in the SDM.

Conclusions

With this study, we are able to elucidate the origin of the high electromechanical properties of BT in the grain size range around 1 µm. The high domain wall density and mobility play a crucial role and define the grain size range of the maximum in properties. The applied electric field induces a phase transformation, which was already reported in the literature[10,24,43,44]. Despite insufficient experimental resolution to determine the induced phase symmetry, Ghosh *et al.*[10] presented a robust and structured data set that corroborates the conclusions of this paper. In agreement with their model, the volume fraction of the induced phase is responsible for the enhancement in field induced strain for this grain size. Here, we clarify for the first time the nature of this field induced phase transformation to be from tetragonal to orthorhombic. The *in situ* synchrotron experiments with high angular resolution prove this unambiguously. Domain wall density and mobility together with phase transformation constitute the origin of the maxima in properties in the grain size range around 1 µm. The results allow a deeper understanding of the electric field induced response in the model system barium titanate and underline the importance of phase transformations for high electromechanical

properties. This knowledge provides the basis for new guidelines to develop and tailor new advanced functional electroceramics. Direct experimental evidence of the coexistence of morphotropic phase boundary-type phases in a ferroelectric compound such as BT indicates that this can occur in similar compounds.

Supplementary Material

See supplementary material for details on the lattice parameters and the incompatibilities between the surface and the interior of the sample. Details are also provided on the lack of angular resolution of the 2D detector in the in situ high energy X-ray diffraction experiments to determine the electric field induced phase symmetry. And finally the two-dimensional graphical construction of the measured and refined data correlating ω and 2θ for the 110_C reflection under a 2 kV/mm electric field applied to the sample.

Acknowledgment

The authors would like to thank the *Deutscher Akademischer Austauschdienst* (DAAD, Bonn, Germany) for scholarship funding and the *Deutsche Forschungsgemeinschaft* (DFG) for funding under grant number HI 1867/1-2. We acknowledge DESY (Hamburg, Germany), a member of the Helmholtz Association HGF, for the provision of experimental facilities. Parts of this research were carried out at beamline P02.1. Beamtime was allocated for proposals I-20191018 and I-20210624.

Author contributions

L.L.d.S. prepared the samples. L.L.d.S., K.-Y.L., M.H. (Manuel Hinterstein), M.E., A.S. and L.K.V. performed the *in situ* high energy X-ray diffraction experiments. S.P., C.G.C., N.O.d.S. and G.P. performed a computational microstructure analysis of the samples. C.G.C. developed the scripts for quick evaluation of the electromechanical experiments. M.H. (Manuel Hinterstein) performed the refinement of the X-ray diffraction data. G.P. critically commented on the results, the data analysis, and the text. M.J.H. (Michael J. Hoffmann) supervised the processing of the samples and provided valuable directions. L.L.d.S. and M.H. (Manuel Hinterstein) wrote the paper with contribution from all authors.

Competing interests

The authors declare no competing interests.

Data Availability Statement

The data that support the findings of this study are available within this article and its supplementary material.

References

1. Acosta, M. *et al.* BaTiO3-based piezoelectrics: Fundamentals, current status, and perspectives. *Appl. Phys. Rev.* **4**, (2017).

2. Haertling, G. H. Ferroelectric Ceramics; History and Technology.pdf. **818**, (1999).

3. Hinterstein, M. *et al.* Determining fundamental properties from diffraction: Electric field induced strain and piezoelectric coefficient. *Phys. Rev. B* **99**, 1–6 (2019).

4. Hinterstein, M. *et al.* Interplay of strain mechanisms in morphotropic piezoceramics. *Acta*

494 *Mater.* **94**, 319–327 (2015).

4955. Daniels, J. E., Picht, G., Kimber, S. & Webber, K. G. Mechanical double loop behavior in
496 BaTiO3: Stress induced paraelastic to ferroelastic phase transformation. *Appl. Phys. Lett.* **103**,
497 (2013).

4986. BUESSEM, W. R., CROSS, L. E. & GOSWAMI, A. K. Phenomenological Theory of High
499 Permittivity in Fine-Grained Barium Titanate. *J. Am. Ceram. Soc.* **49**, 33–36 (1966).

5007. Kinoshita, K. & Yamaji, A. Grain-size effects on dielectric properties in barium titanate
501 ceramics. *J. Appl. Phys.* **47**, 371–373 (1976).

5028. Buscaglia, V. & Randall, C. A. Size and scaling effects in barium titanate. An overview. *J. Eur.*
503 *Ceram. Soc.* 0–1 (2020). doi:10.1016/j.jeurceramsoc.2020.01.021

5049. Picht, G. *et al.* Grain size effects in donor doped lead zirconate titanate ceramics. *J. Appl. Phys.*
505 **128**, 214105 (2020).

50610. Ghosh, D. *et al.* Domain wall displacement is the origin of superior permittivity and
507 piezoelectricity in BaTiO3 at intermediate grain sizes. *Adv. Funct. Mater.* **24**, 885–896 (2014).

50811. Huibregtse, E. J. & Young, D. R. Triple Hysteresis Loops and the Free-Energy Function in the
509 Vicinity. *Phys. Rev.* **103**, 1705–1711 (1956).

51012. Merz, W. J. The electric and optical behavior of BaTiO3 single-domain crystals. *Phys. Rev.* **76**,
511 1221–1225 (1949).

51213. Diamond, H. Variation of permittivity with electric field in perovskite-like ferroelectrics. *J.*
513 *Appl. Phys.* **32**, 909–915 (1961).

51414. Arlt, G., Hennings, D. & De With, G. Dielectric properties of fine-grained barium titanate
515 ceramics. *J. Appl. Phys.* **58**, 1619–1625 (1985).

51615. Bäurer, M. *et al.* Abnormal grain growth in undoped strontium and barium titanate. *Acta*
517 *Mater.* **58**, 290–300 (2010).

51816. Lee, B. K., Chung, S. Y. & Kang, S. J. L. Grain boundary faceting and abnormal grain growth in
519 BaTiO3. *Acta Mater.* **48**, 1575–1580 (2000).

52017. BURKE, J. E. Role of Grain Boundaries in Sintering. *J. Am. Ceram. Soc.* **40**, 80–85 (1957).

52118. Karaki, T., Yan, K., Miyamoto, T. & Adachi, M. Lead-free piezoelectric ceramics with large
522 dielectric and piezoelectric constants manufactured from BaTiO3 nano-powder. *Japanese J.*
523 *Appl. Physics, Part 2 Lett.* **46**, 3–5 (2007).

52419. Maiwa, H. Electromechanical properties of BaTiO3 ceramics prepared by spark plasma
525 sintering and other methods. *Jpn. J. Appl. Phys.* **48**, (2009).

52620. Takeuchi, T., Tabuchi, M., Kageyama, H. & Suyama, Y. Preparation of dense BaTiO3 ceramics
527 with submicrometer grains by spark plasma sintering. *J. Am. Ceram. Soc.* **82**, 939–943 (1999).

52821. Curecheriu, L., Buscaglia, M. T., Buscaglia, V., Zhao, Z. & Mitoseriu, L. Grain size effect on the
529 nonlinear dielectric properties of barium titanate ceramics. *Appl. Phys. Lett.* **97**, 1–4 (2010).

53022. Kim, B. C., Chae, K. W. & Cheon, C. Il. Effect of Sintering Temperature on the Ferroelectric
531 Properties and the Electro-caloric Effect in Barium-Titanate Ceramics. *J. Korean Phys. Soc.* **76**,
532 226–230 (2020).

53323. OPPOLZER, H. & SCHMELZ, H. Investigation of Twin Lamellae in BaTiO3 Ceramics. *J. Am.*
534 *Ceram. Soc.* **66**, 444–446 (1983).

53524. Wang, Z., Webber, K. G., Hudspeth, J. M., Hinterstein, M. & Daniels, J. E. Electric-field-induced
536 paraelectric to ferroelectric phase transformation in prototypical polycrystalline $BaTiO_3$. *Appl.*
537 *Phys. Lett.* **105**, 161903 (2014).

53825. Schader, F. H., Aulbach, E., Webber, K. G. & Rossetti, G. A. Influence of uniaxial stress on the
539 ferroelectric-to-paraelectric phase change in barium titanate. *J. Appl. Phys.* **113**, 174103
540 (2013).

54126. Franzbach, D. J., Gu, Y. J., Chen, L. Q. & Webber, K. G. Electric field-induced tetragonal to
542 orthorhombic phase transitions in [110] c -oriented BaTiO 3 single crystals. *Appl. Phys. Lett.*
543 **101**, 232904 (2012).

54427. Lee, K. Y. *et al.* The complex structural mechanisms behind strain curves in bismuth sodium
545 titanate-barium titanate. *Appl. Phys. Lett.* **116**, (2020).

54628. Lee, K.-Y. *et al.* Electric-Field-Induced Phase Transformation and Frequency-Dependent
547 Behavior of Bismuth Sodium Titanate–Barium Titanate. *Materials (Basel).* **13**, 1054 (2020).

54829. Paterson, A. R. *et al.* Relaxor-ferroelectric transitions: Sodium bismuth titanate derivatives.
549 *MRS Bull.* **43**, 600–606 (2018).

55030. Hinterstein, M. *et al.* Cyclic electric field response of morphotropic $Bi_{1/2}Na_{1/2}TiO_3$-$BaTiO_3$
551 piezoceramics. *Appl. Phys. Lett.* **106**, 222904 (2015).

55231. Hinterstein, M. *et al.* Field-induced phase transition in Bi 1/2 Na 1/2 TiO 3 -based lead-free
553 piezoelectric ceramics. *J. Appl. Crystallogr.* **43**, 1314–1321 (2010).

55432. Daniels, J. E., Jo, W., Rödel, J. & Jones, J. L. Electric-field-induced phase transformation at a
555 lead-free morphotropic phase boundary: Case study in a 93%(Bi[sub 0.5]Na[sub 0.5])TiO[sub
556 3]–7% BaTiO[sub 3] piezoelectric ceramic. *Appl. Phys. Lett.* **95**, 32904 (2009).

55733. Hinterstein, M. *et al.* Structural Description of the Macroscopic Piezo- and Ferroelectric
558 Properties of Lead Zirconate Titanate. *Phys. Rev. Lett.* **107**, 077602 (2011).

55934. Hinterstein, M. *et al.* Structural contribution to the ferroelectric fatigue in lead zirconate
560 titanate ceramics. *Phys. Rev. B* **90**, 094113 (2014).

56135. Franzbach, D. J. *et al.* Electric-field-induced phase transitions in co-doped Pb(Zr 1–x Ti x)O 3 at
562 the morphotropic phase boundary. *Sci. Technol. Adv. Mater.* **15**, 015010 (2014).

56336. Mgbemere, H. E., Schneider, G. A., Schmitt, L. A. & Hinterstein, M. Electric field induced phase
564 transition in Mn-doped $(K_{0.48}Na_{0.48}Li_{0.04})NbO_3$ lead-free ceramics. *J. Ceram. Sci. Technol.* **8**, 45–
565 52 (2017).

56637. Iamsasri, T. *et al.* Electric field-induced phase transitions in Li-modified Na0.5K0.5NbO3 at the
567 polymorphic phase boundary. *J. Appl. Phys.* **117**, 0–7 (2015).

56838. Lee, M. K., Yang, S. A., Park, J. J. & Lee, G. J. Proposal of a rhombohedral-tetragonal phase
569 composition for maximizing piezoelectricity of (K,Na)NbO 3 ceramics. *Sci. Rep.* **9**, 1–7 (2019).

57039. Hayati, R., Bahrevar, M. A., Ganjkhanlou, Y., Rojas, V. & Koruza, J. Electromechanical
571 properties of Ce-doped (Ba0.85Ca0.15)(Zr0.1Ti0.9)O3 lead-free piezoceramics. *J. Adv. Ceram.*
572 **8**, 186–195 (2019).

57340. Keeble, D. S., Benabdallah, F., Thomas, P. A., Maglione, M. & Kreisel, J. Revised structural
574 phase diagram of (Ba0.7Ca 0.3TiO3)-(BaZr0.2Ti0.8O3). *Appl. Phys. Lett.* **102**, 1–6 (2013).

57541. Zhang, M. H. *et al.* Electric-field-induced antiferroelectric to ferroelectric phase transition in
576 polycrystalline NaNbO3. *Acta Mater.* **200**, 127–135 (2020).

57742. Zhang, M. H. *et al.* Revealing the mechanism of electric-field-induced phase transition in antiferroelectric NaNbO3by in situ high-energy x-ray diffraction. *Appl. Phys. Lett.* **118**, (2021).

57943. Wada, S. *et al.* Enhanced piezoelectric property of barium titanate single crystals with engineered domain configurations. *Japanese J. Appl. Physics, Part 1 Regul. Pap. Short Notes Rev. Pap.* **38**, 5505–5511 (1999).

58244. Kalyani, A. K. *et al.* Metastable monoclinic and orthorhombic phases and electric field induced irreversible phase transformation at room temperature in the lead-free classical ferroelectric BaTiO3. *Phys. Rev. B - Condens. Matter Mater. Phys.* **91**, 1–12 (2015).

58545. Zhao, Z. *et al.* Grain-size effects on the ferroelectric behavior of dense nanocrystalline <math display="inline"> <mrow> <msub> <mrow> <mi mathvariant="normal">BaTiO</mi> </mrow> <mn>3</mn> </msub> </mrow> </math> ceramics. *Phys. Rev. B* **70**, 024107 (2004).

58846. Hoshina, T. *et al.* Domain size effect on dielectric properties of barium titanate ceramics. *Jpn. J. Appl. Phys.* **47**, 7607–7611 (2008).

59047. Hoshina, T., Kigoshi, Y., Hatta, S., Takeda, H. & Tsurumi, T. Domain contribution to dielectric properties of fine-grained BaTiO 3 ceramics. *Jpn. J. Appl. Phys.* **48**, (2009).

59248. Huan, Y., Wang, X., Fang, J. & Li, L. Grain size effect on piezoelectric and ferroelectric properties of BaTiO3 ceramics. *J. Eur. Ceram. Soc.* **34**, 1445–1448 (2014).

59449. Frey, M. H., Xu, Z., Han, P. & Payne, D. A. Role of interfaces on an apparent grain size effect on the dielectric properties for ferroelectric barium titanate ceramics. *Ferroelectrics* **206–207**, 337–353 (1998).

59750. Kim, H. T. & Han, Y. H. Sintering of nanocrystalline BaTiO3. *Ceram. Int.* **30**, 1719–1723 (2004).

59851. Chen, I. W. & Wang, X. H. Sintering dense nanocrystalline ceramics without final-stage grain growth. *J. Prosthodont.* **404**, 168–171 (2000).

60052. Kong, S., Kumar, N., Checchia, S., Cazorla, C. & Daniels, J. E. Defect-Driven Structural Distortions at the Surface of Relaxor Ferroelectrics. *Adv. Funct. Mater.* **29**, 1900344 (2019).

60253. Dippel, A. C. *et al.* Beamline P02.1 at PETRA III for high-resolution and high-energy powder diffraction. *J. Synchrotron Radiat.* **22**, 675–687 (2015).

60454. Herklotz, M. *et al.* Advances in in situ powder diffraction of battery materials: a case study of the new beamline P02.1 at DESY, Hamburg. *J. Appl. Crystallogr.* **46**, 1117–1127 (2013).

60655. Lee, K. *et al.* Electric-Field-Induced Phase Transformation and. **3**, 1–14 (2020).

60756. Schökel, A. *et al.* Multi-analyser detector (MAD) for high-resolution and high-energy powder X-ray diffraction. *J. Synchrotron Radiat.* **28**, 146–157 (2021).

60957. Sapkota, P. *et al.* Influence of grain size effect and Ba/Ti ratios on dielectric, ferroelectric, and piezoelectric properties of BaTiO3 ceramics. *Jpn. J. Appl. Phys.* **58**, (2019).

61158. Polotai, A. V., Ragulya, A. V. & Randall, C. A. Preparation and size effect in pure nanocrystalline barium titanate ceramics. *Ferroelectrics* **288**, 93–102 (2003).

61359. Birch, F. Finite Elastic Strain of Cubic Crystals. *Phys. Rev.* **71**, 809–824 (1947).

61460. Pruzan, P. *et al.* Equation of state of BaTiO3 and KNbO3 at room temperature up to 30 GPa. *Solid State Commun.* **123**, 21–26 (2002).

61661. Schultheiß, J. *et al.* Quantitative mapping of nanotwin variants in the bulk. *Scr. Mater.* **199**, 4–8 (2021).

61862. Schökel, A. *et al*. Multi Analyser Detector (MAD) for High Resolution and High Energy Powder
619 X-ray Diffraction. *J. Synchrotron Radiat*. in print (2020). doi:10.1107/S1600577520013223

62063. Hinterstein, M. *et al*. Influence of lanthanum doping on the morphotropic phase boundary of
621 lead zirconate titanate. *J. Appl. Phys.* **108**, (2010).

62264. Daniels, J. E., Jones, J. L. & Finlayson, T. R. Characterization of domain structures from
623 diffraction profiles in tetragonal ferroelastic ceramics. *J. Phys. D. Appl. Phys.* **39**, 5294–5299
624 (2006).

62565. Schader, F. H., Khakpash, N., Rossetti, G. A. & Webber, K. G. Phase transitions in BaTiO3 under
626 uniaxial compressive stress: Experiments and phenomenological analysis. *J. Appl. Phys.* **121**,
627 (2017).

62866. Arlt, G., Dederichs, H. & Herbiet, R. 90°-Domain wall relaxation in tetragonally distorted
629 ferroelectric ceramics. *Ferroelectrics* **74**, 37–53 (1987).

63067. Arlt, G. & Pertsev, N. A. Force constant and effective mass of 90°domain walls in ferroelectric
631 ceramics. *J. Appl. Phys.* **70**, 2283–2289 (1991).

63268. Herbiet, R., Robels, U., Dederichs, H. & Arlt, G. Domain Wall And Volume Contributions To
633 Material Properties Of Pzt Ceramics. *Ferroelectrics* **98**, 107–121 (1989).

63469. Hinterstein, M. *et al*. Field-induced phase transition in $Bi_{1/2}Na_{1/2}TiO_3$ -based lead-free
635 piezoelectric ceramics. *J. Appl. Crystallogr.* **43**, 1314–1321 (2010).

63670. Acosta, M. *et al*. Piezoelectricity and rotostriction through polar and non-polar coupled
637 instabilities in bismuth-based piezoceramics. *Sci. Rep.* **6**, 28742 (2016).

63871. Damjanovic, D. A morphotropic phase boundary system based on polarization rotation and
639 polarization extension. *Appl. Phys. Lett.* **97**, 1–3 (2010).

64072. Damjanovic, D. Comments on origins of enhanced piezoelectric properties in ferroelectrics.
641 *IEEE Trans. Ultrason. Ferroelectr. Freq. Control* **56**, 1574–1585 (2009).

642